Journal of Physics D: Applied Physics

PAPER

Imidazole ionic liquids-based ultra-broadband metamaterial absorbers from cross-architecture design

To cite this article: Yongji Guan *et al* 2024 *J. Phys. D: Appl. Phys.* **57** 135504

IOP Publishing
Journal of Physics D: Applied Physics
J. Phys. D: Appl. Phys. **57** (2024) 135504 (10pp)
https://doi.org/10.1088/1361-6463/ad18f3

Imidazole ionic liquids-based ultra-broadband metamaterial absorbers from cross-architecture design

Yongji Guan[1], **Xiaoxiang Li**[1], **Jiahong Zou**[1], **Jiajun Fan**[1], **Fulong Yang**[2] **and Xiaoping Zhang**[1,*]

[1] Institute of Optoelectronics and Electromagnetic Information, School of Information Science and Engineering, Lanzhou University, Lanzhou 730000, People's Republic of China
[2] College of Electrical and Information Engineering, Lanzhou University of Technology, Lanzhou 730050, People's Republic of China

E-mail: zxp@lzu.edu.cn

Received 31 August 2023, revised 26 November 2023
Accepted for publication 26 December 2023
Published 5 January 2024

Abstract

Room temperature ionic liquids (ILs) characterized by high dielectric loss factors and conductivity emerge as promising candidates for liquid-based metamaterial absorbers (LMMAs). In this work, the IL 1-ethyl-3-methyl-imidazolium dicyanamide was employed to construct an IL-based LMMA, leveraging a cross-architecture (C-A) design paradigm. Numerical analyses reveal that the C-A ILMMA achieves an absorption efficiency exceeding 90% within the frequency range of 7.5–57.8 GHz, translating to a relative absorption bandwidth of 153%. Moreover, the symmetrical configuration of the C-A ILMMA ensures its robust performance across a comprehensive range of polarization angles (0° to 90°), thereby underscoring its polarization insensitivity. Even with an increased incident angle of 60°, the C-A ILMMA sustains an absorption rate above 85% within the frequency intervals of 9.0–13.3 GHz and 24.7–60.0 GHz, highlighting its broad incident angle absorption capability. Owing to the superior thermal stability of the IL, the C-A ILMMA consistently maintains an absorption rate of over 90% across a temperature gradient from 20 °C to 100 °C. Mechanistic investigations reveal that the optimal absorption of the C-A ILMMA predominantly stems from dielectric polarization loss and the ionic current induced within the ILs. Subsequent experimental evaluations corroborate that the C-A ILMMA exhibits an absorptivity in excess of 90% over an ultra-broadband frequency spanning 10–40 GHz, aligning closely with numerical predictions. This IL-based C-A ILMMA not only augments the absorption bandwidth substantially but also enhances the adaptability of ILMMA in more rigorous environments, attributed to the commendable physicochemical properties of ILs.

Keywords: liquid-based metamaterial absorbers, ionic liquids, cross-architecture design, ultra-broadband

1. Introduction

Liquid-based metamaterial absorbers (LMMAs) have garnered significant interest due to their cost-effective reconstruction and tunability [1, 2]. By modulating the liquid's shape and thickness, absorption bands can be controlled, offering an advantage over solid-based MMAs [3–5], which often rely on electromagnetic resonance [6, 7] enabled by programmable controls [7, 8], leading to the widespread application in photoelectric conversion, on-chip system and photonic and plasmonic metasensors [9–11]. This adaptability paves the way for potential applications in optically transparent absorbers and transparent energy harvesting systems [12–14].

---

[*] Author to whom any correspondence should be addressed.

Yoo *et al* [15] pioneered the use of common liquid water as an absorbing material, presenting a water droplet-based MMA that achieved an average absorption of over 91% in a wide frequency range of 10.0 GHz with a water drop thickness of 2.5 mm. Subsequent research has delved into water-based LMMAs, exploring various attributes such as optical transparency [12–14, 16, 17], shape adaptability [13, 14, 18, 19], thermal properties [20–24], ionic characteristics [25], polarization [26, 27], temperature insensitivity [28], ultra-broadband [29–31], wide incident angle [26, 27, 32] and multiple functions [13, 14, 16]. However, the liquid water employed in these studies has inherent limitations, including volatility, limited thermostability, low electrical conductivity, and a narrow electrochemical stability window. These constraints potentially hinder the broader application of LMMAs in both civilian and military products under extreme conditions.

Room temperature ionic liquids (ILs), as an emerging class of functional liquids typically composed of bulky organic cations and inorganic or organic anions, present a promising alternative. Their broad temperature range, recyclability, thermal stability, and ionic conductivity [33–36] make them suitable candidates for LMMAs [37–40]. Gong and Yang *et al* [37, 38] conducted experimental measurements on several imidazole ILs with varying anions and cations. They systematically assessed their absorption properties across frequencies from 1.0 to 50.0 GHz, attributing the microwave absorption of these ILs to their high conductive and dielectric loss. Building on this foundation, Gong *et al* [37] introduced 1-ethyl-3-methylimidazolium dicyanamide ([Emim][N(CN)$_2$]) to an MMA, achieving robust microwave absorption exceeding 90% in the 8.4–29.0 GHz range with a total thickness of 4.036 mm. To enhance impedance characteristics, Yang *et al* [39] incorporated a top dielectric cover, resulting in an ultra-broadband ILMMA with over 90% absorption in the 9.3–49.0 GHz range. This ILMMA also demonstrated polarization insensitivity and a wide incidence angle. Remove the metallic ground to block the propagation of electromagnetic waves, Yang *et al* [40] used 1-ethyl-3-methylimidazolium tetrafluoroborate to create an all-dielectric ultra-broadband ILMMA. This design achieved over 90% absorption from 13.9 to 50.0 GHz, functioning effectively across a spectrum of polarization angles (0°–90°) and incident angles (0°–60°).

In the aforementioned ILMMAs, a consistent design element was the single cylindrical groove unit cell with uniform height in the periodic array [37, 39, 40]. To enhance the absorption range and economize on IL usage, we introduced photosensitive resin rings and selected two distinct cylindrical groove heights for the unit cell. As depicted in figure 1, uniform height grooves are diagonally positioned, while those with varied heights align on one side. This design is termed as the cross-architecture ILMMA (C-A ILMMA). Incorporating the high dielectric loss and conductivity IL [Emim][N(CN)$_2$], both numerical and experimental evaluations revealed that the C-A ILMMA achieved over 90% absorption between 7.5–57.8 GHz, boasting a relative absorption bandwidth of 153%. The symmetrical design ensures effective performance across all polarization angles (0°–90°), maintaining absorption rates above 85% between 9.0–13.3 GHz and 24.7–60.0 GHz, even at an incident angle of 60°.

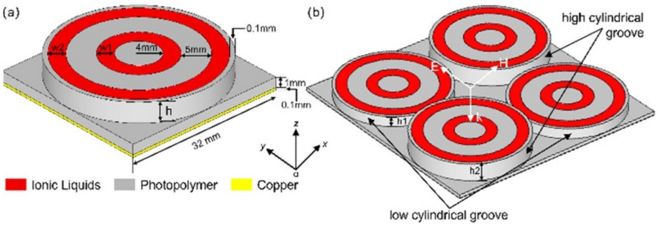

Figure 1. Illustration of the structural design: (a) depicts the single cylindrical groove, and (b) presents the schematic representation of the unit cell within the C-A ILMMA.

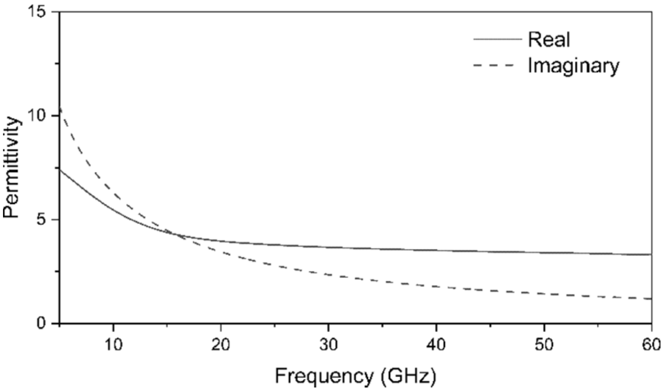

Figure 2. The frequency-dispersive permittivity of the IL [Emim][N(CN)$_2$].

2. Simulation and numerical analysis

The proposed unit cell design for the C-A ILMMA is illustrated in figure 1. As depicted in figure 1(a), the grey cylindrical groove, integrated with a substrate, is composed of the photosensitive resin 8000, which possesses a dielectric constant of 3(1-0.02i). This structure is supported by a copper ground plane, 36 μm in thickness, with a conductivity of 5.8×10^7 S m^{-1}. This ground plane serves to obstruct the propagation of electromagnetic waves. The inner and outer rings, highlighted in red in figure 1(a), represent the IL [Emim][N(CN)$_2$]. This IL, characterized by its frequency-dispersive permittivity (figure 2), is selected as the liquid absorbing material for the C-A ILMMA due to its lower reflection loss characteristics (S_{11}) and enhanced dielectric loss factor and conductivity (2.8 S m^{-1}) at ambient temperature. The widths of the inner and outer rings, composed of photosensitive resin, are designated as 5 mm and 0.1 mm, respectively, while the radius of the central cylindrical photosensitive resin is set to 4 mm. In figure 1(b), the heights of the individual cylindrical grooves within the unit cell are denoted as $h1$ and $h2$, respectively. The substrate, made of photosensitive resin, has a consistent height of 1 mm. The widths of the inner and outer IL rings are specified as $w1$ and $w2$, respectively.

Numerical simulations were conducted utilizing the finite integration technique, spanning a frequency range of 5–60 GHz. For the unit cell, periodic boundary conditions were imposed on the $x-y$ plane, while open boundary conditions were applied in the z direction. The incident electromagnetic wave, characterized as a uniform plane wave, propagated along the $-z$ direction, with the electric field vector's polarization aligned with the y axis. The electromagnetic absorptivity (A) of the C-A ILMMA is defined by:

$$A(w) = 1 - R(w) - T(w) \tag{1}$$

where the $A(\omega)$, $R(\omega)$ and $T(\omega)$ represent the absorptivity, reflectivity and transmissivity respectively.

Given the reflection and transmission losses, the $R(\omega)$ and $T(\omega)$ can be expressed as:

$$R(w) = |S_{11}|^2 \tag{2}$$

$$T(w) = |S_{21}|^2 \tag{3}$$

where the S_{11} and S_{21} denote the reflection and transmission coefficients, respectively. Consequently, the $A(\omega)$ can be reformulated as:

$$A(w) = 1 - |S_{11}|^2 - |S_{21}|^2. \tag{4}$$

Considering the complete obstruction of transmission by the copper ground plane, the transmission coefficient S_{21} becomes zero. Thus, the final expression for absorptivity $A(\omega)$ simplifies to:

$$A(w) = 1 - |S_{11}|^2. \tag{5}$$

In this work, the absolute absorption bandwidth is defined as:

$$B = \Delta f = f_{\mathrm{H}} - f_{\mathrm{L}} \tag{6}$$

where the f_{H} and f_{L} represent the upper and lower frequency limits, respectively, at which the absorption efficiency exceeds 90%.

Therefore, the relative absorption bandwidth is defined as the quotient of absolute bandwidth and the center frequency (f_{C}):

$$B_{\mathrm{R}} = \frac{B}{f_{\mathrm{C}}} \tag{7}$$

where center frequency is usually defined as the arithmetic mean of the upper and lower frequencies so that:

$$f_{\mathrm{C}} = \frac{f_{\mathrm{H}} + f_{\mathrm{L}}}{2}. \tag{8}$$

Thus the B_{R} can be reformulated as:

$$B_{\mathrm{R}} = \frac{2(f_{\mathrm{H}} - f_{\mathrm{L}})}{f_{\mathrm{H}} + f_{\mathrm{L}}}. \tag{9}$$

The power loss is defined as:

$$P_{\mathrm{loss}} = \frac{1}{2}\sigma\left|\vec{E}(f_0)\right|^2 \tag{10}$$

where σ, $\vec{E}$ and f_0 represent the conductivity, electric field and frequency respectively.

3. Results and discussion

3.1. Optimization of geometrical structure parameters

As shown in figure 1, the heights of the individual cylindrical grooves within the unit cell ($h1$ and $h2$) and widths of the inner and outer IL rings ($w1$ and $w2$) are variable. Therefore, in this section, these four parameters are optimized to maximize the absorption efficiency and absorption bandwidth of the C-A ILMMA while minimizing the usage of IL. Firstly, to ascertain the optimal geometrical structure parameters, we commenced by examining the influence of the cylindrical groove heights, $h1$ and $h2$, on the absorption performance of ILMMA. Six distinct combinations were considered, with $h1$ and $h2$ ranging from 3 mm and 5 mm, while maintaining the widths of the inner and outer IL rings at $w1 = w2 = 3$ mm.

Figure 3 presents the absorption performance of the ILMMA for the six height combinations. It is evident that the C-A ILMMA outperforms configurations with uniform heights for $h1$ and $h2$. Furthermore, among the configurations assessed, the C-A ILMMA with $h1 = 3$ mm and $h2 = 5$ mm exhibited a broader effective absorption band (exceeding 90%) compared to the combinations of $h1 = 3$ mm with $h2 = 4$ mm and $h1 = 3$ mm with $h2 = 5$ mm. This confirms that the absorption performance of the C-A design is better than that of the use cylindrical groove unit cells with the same height in the periodic array. Consequently, the configuration with $h1 = 3$ mm and $h2 = 5$ mm was selected for subsequent parameter optimization.

Subsequently, we explored the influence of the widths $w1$ and $w2$ of the IL in the inner and outer rings on the absorption performance of the C-A ILMMA, maintaining the cylindrical groove heights at $h1 = 3$ mm and $h2 = 5$ mm. Initially, with $w2$ fixed at 3 mm, $w1$ was varied between 1 mm and 5 mm. As illustrated in figure 4(a), an augmentation in $w1$ enhances the absorption performance of the C-A ILMMA, as evidenced by both the effective absorption bandwidth and the absorption rate surpassing 90%. However, when $w1$ extends to 5 mm, a dip in absorption, falling below 90% between 43.1 GHz and 43.7 GHz, is observed. Balancing IL consumption and absorption performance, $w1 = 3$ mm was deemed optimal for subsequent optimization.

In the next phase, while retaining $h1 = 3$ mm, $h2 = 5$ mm, and $w1 = 3$ mm, the absorption performance of the C-A ILMMA was optimized by varying $w2$ from 1 mm to 5 mm. Figure 4(b) reveals that with an increase in $w2$, the C-A ILMMA consistently delivers superior absorption, achieving a broad absorption bandwidth. However, for $w2$ values of 4 mm or greater, absorption dips below 90% in the 44.1–45.4 GHz range. Taking into account both IL dosage and absorption

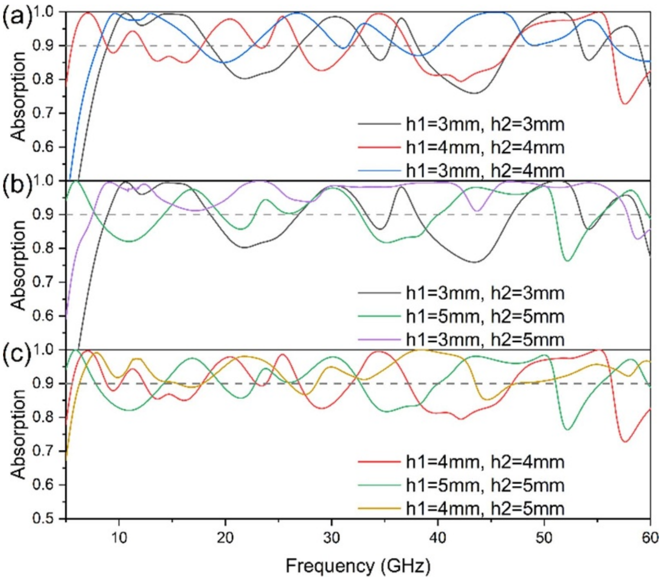

Figure 3. Absorption spectra of the C-A ILMMA, showcasing variations across six distinct height combinations for h1 and h2.

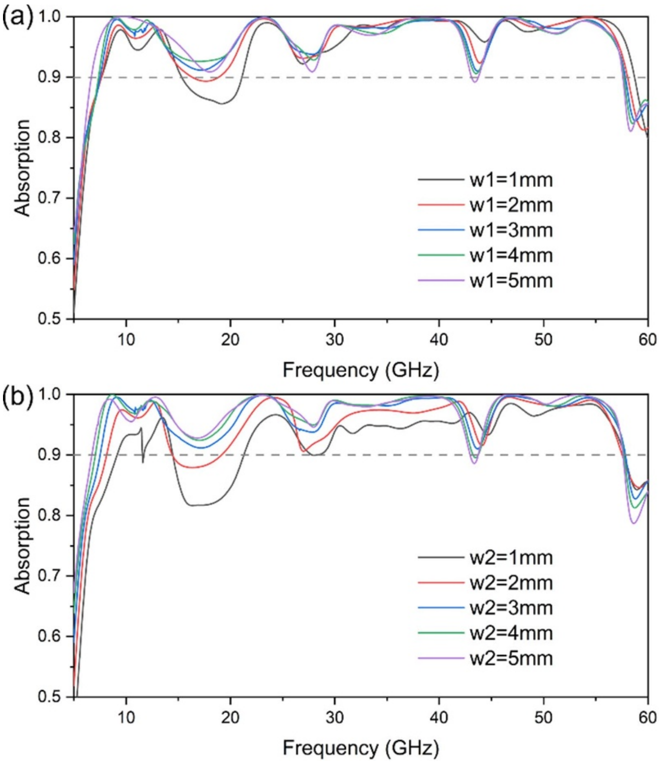

Figure 4. Absorption spectra of the C-A ILMMA under two conditions: (a) with varying width w1 of the IL in the inner ring, and (b) with varying width $w2$ of the IL in the outer ring. The cylindrical groove heights are maintained at $h1 = 3$ mm and $h2 = 5$ mm.

performance, $w2 = 3$ mm emerged as the optimal parameter. Consequently, the ideal structural parameters for the C-A ILMMA are determined to be $h1 = 3$ mm, $h2 = 5$ mm, and $w1 = w2 = 3$ mm.

From the preceding analysis, the selected C-A ILMMA configuration demonstrates an effective absorption rate exceeding 90% within the 7.5–57.8 GHz frequency range. Additionally, the absorption peaks of the C-A ILMMA are prominently centered at 9.1 GHz, 12.4 GHz, 23.2 GHz, 30.3 GHz, 40.5 GHz, 46.8 GHz, and 54.2 GHz, respectively. Honestly, we acknowledge that the currently selected parameters are the most suitable but still fall short of being ideal because optimizing one parameter necessitates the fixation of others. Therefore, achieving optimal parameters without fixing any of them remains a future objective.

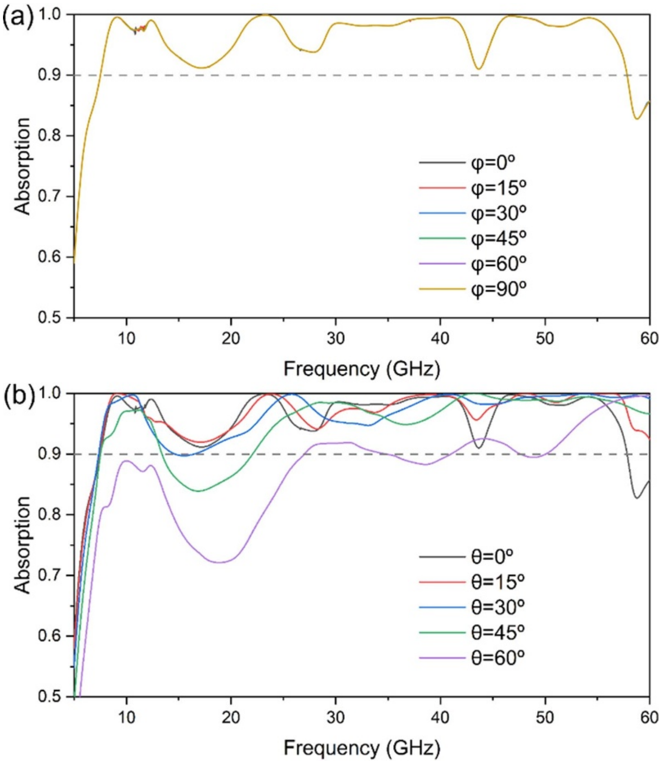

Figure 5. Absorption spectra of the C-A ILMMA under varying conditions: (a) across polarization angles ranging from 0° to 90°, and (b) for incidence angles spanning from 0° to 60°.

3.2. *Influence of polarization and incident angle*

Furthermore, we assessed the impact of both the incident and polarization angles on the absorption performance of the C-A ILMMA. As depicted in figure 5(a), the C-A ILMMA demonstrates a notable insensitivity to polarization due to the rotational symmetry of the structure, maintaining its performance as the polarization angle spans from 0° to 90°. Figure 5(b) presents the absorption spectra of the C-A ILMMA as the incident angle shifts from 0° to 60°. Notably, while there is a marked decline in the absorption rate with increasing incident angles, the C-A ILMMA continues to showcase robust broadband absorption, even when the incident angle approaches 45°, which could be attributed to the fact that more electromagnetic waves are reflected and less electromagnetic energy is consumed by the C-A ILMMA.

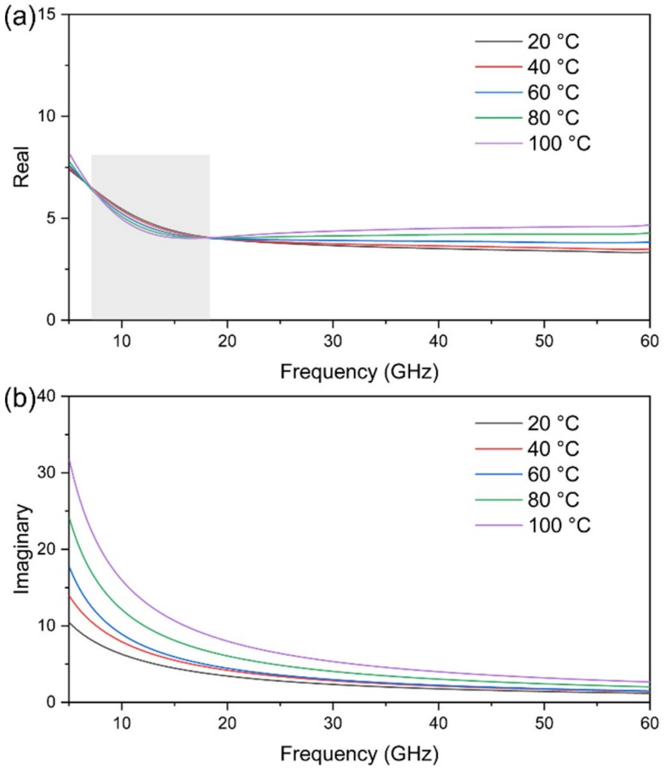

Figure 6. The real (a) and imaginary (b) part of permittivity of the IL [Emim][N(CN)$_2$] at temperature from 20 °C to 100 °C, where the shaded region ranges from 7 GHz to 19 GHz.

3.3. *Effect of temperature*

It is well-known that the temperature has a great influence on dielectric properties of ILs [38, 41, 42]. The temperature-dependent permittivity of the IL [Emim][N(CN)$_2$] demonstrates an increase in the imaginary part of permittivity with rising temperature, as depicted in figure 6(b). The real part of permittivity presented in figure 6(a) also increased with increasing temperature except for the frequency range between 7 GHz and 19 GHz. The imaginary part values depend on conductance and polarization, revealing that the amplified low-frequency band was significantly higher than the high-frequency band. The low-frequency band is chiefly affected by conductivity loss, whereas the high-frequency bands are mainly impacted by polarization loss. This phenomenon may be due to the decreased viscosity of ions and the increased mobility of free ions and ion clusters with rising temperatures.

Consequently, we examined the impact of temperature variations on the absorption performance of the C-A ILMMA. As illustrated in figure 7, while there is a discernible decrease in the absorption rate of the absorber between 9.1 GHz and 12.4 GHz as the temperature rises from 20 °C to 100 °C, the absorption rate consistently remains above 90%. This results could be ascribed to the decreasing real part of the permittivity of the IL [Emim][N(CN)$_2$] as temperature rises within this frequency range. Furthermore, a slight expansion in the absorption bandwidth is observed with increasing temperature. Analyzing the absorber's performance across different temperatures, it can be inferred that the C-A ILMMA exhibits temperature insensitivity.

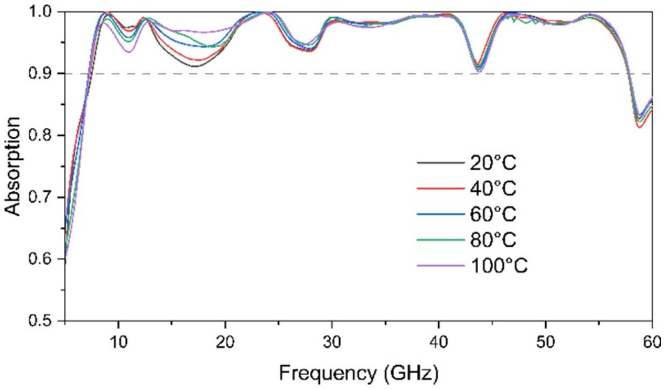

Figure 7. The absorption spectra of the C-A ILMMA at temperature from 20 °C to 100 °C.

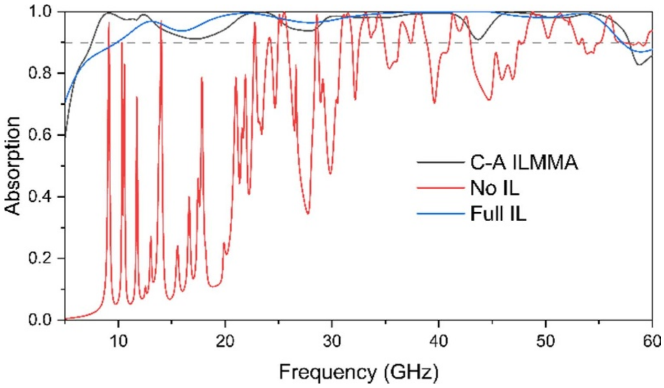

Figure 8. The absorption spectra of the C-A ILMMA, the C-A ILMMA without IL and full IL layer.

3.4. *Absorption mechanism*

The C-A ILMMA is constructed from a periodic array of photosensitive resin 8000 unit cells, complemented by the IL [Emim][N(CN)$_2$]. Both components play pivotal roles in the absorptive capabilities of the C-A ILMMA. As delineated in figure 8, the absorption spectra for the C-A ILMMA, the C-A ILMMA devoid of IL, and the full IL layer reveal that the photosensitive resin alone contributes only modestly to absorption. The primary absorption in the C-A ILMMA is attributed to the IL. However, the significant absorption exhibited by the photosensitive resin at higher frequencies serves to augment the IL's absorption, culminating in the superior absorption performance of the C-A ILMMA.

Owing to the synergistic effects of the periodic photosensitive resin 8000 unit cell and the IL [Emim][N(CN)$_2$], the C-A ILMMA achieves an absorption rate exceeding 90% within the frequency range of 7.5–57.8 GHz. This remarkable performance can be ascribed to the enhanced impedance matching offered by the C-A ILMMA. As illustrated in figure 9, both the real and imaginary components of the ILMMA's equivalent impedance approach values of 1 and 0, respectively.

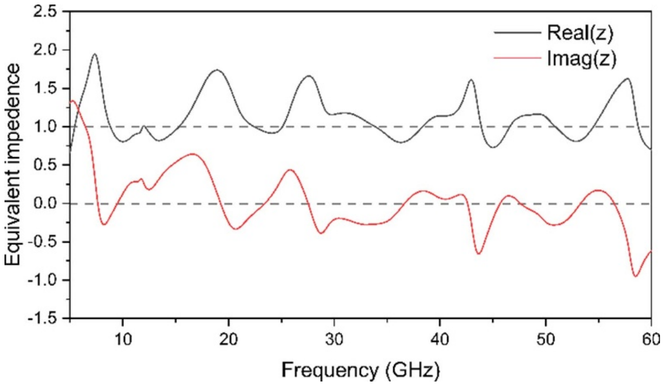

Figure 9. The equivalent impedance of C-A ILMMA.

Such characteristics suggest that, at the macroscopic scale, C-A design can produce various electromagnetic resonances and interference behaviors due to two cylindrical groove with distinct height. Thus, a minimal amount of incident electromagnetic waves is reflected, while a majority are transformed into thermal energy through resonance and interference processes within the material. Whereas at the microscopic scale, the dipole polarization loss from the anion–cation pairs, induced current loss from the movement of the free ions and charged ion clusters, as well as the interface polarization loss between IL, photosensitive resin, and air, which would further dissipate the energy from the incident electromagnetic waves [3–5]. Consequently, the C-A ILMMA serves as an efficient absorber of electromagnetic waves.

To gain a comprehensive understanding of the physical mechanisms responsible for the broadband absorption exhibited by the ultra-broadband C-A ILMMA, we conducted an in-depth analysis of the vector distributions of both magnetic and electric fields, as illustrated in figures 10 and 12, respectively. Additionally, the corresponding power loss density at the peak frequencies was scrutinized according to equation (10), as depicted in figures 11 and 13. From the absorption spectrum presented in figure 5(a), it is evident that distinct absorption peaks are centered at the following frequencies: 9.1 GHz, 12.4 GHz, 23.2 GHz, 30.3 GHz, 40.5 GHz, 46.8 GHz, and 54.2 GHz. These observations strongly suggest the occurrence of resonance phenomena at these specific frequency points.

Remarkably, the unique C-A design of the ILMMA, which incorporates a cylindrical groove containing both inner and outer IL rings, allows for a synergistic contribution from both electrical and magnetic resonances to these absorption peaks, as substantiated by figures 10 and 12. This dual-resonance mechanism distinguishes the C-A ILMMA from previously reported ILMMAs, in which absorption peaks were predominantly influenced by either electrical or magnetic resonance alone [37, 39, 41, 42].

Figure 10 presents the magnetic field distribution within the C-A ILMMA. At the absorption peaks, loop-shaped magnetic field lines emerge, analogous to electric dipoles, thereby inducing electric resonances. The detailed analysis of the magnetic field distribution at each frequency point is given below:

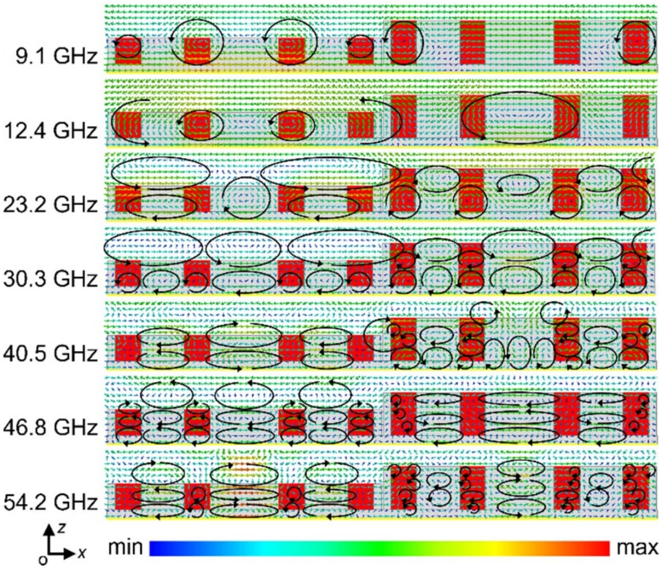

Figure 10. The magnetic field distribution of the C-A ILMMA at the peak frequency of 9.1 GHz, 12.4 GHz, 23.2 GHz, 30.3 GHz, 40.5 GHz, 46.8 GHz and 54.2 GHz respectively in *x–z* cutting planes along with the magnetic field orientation.

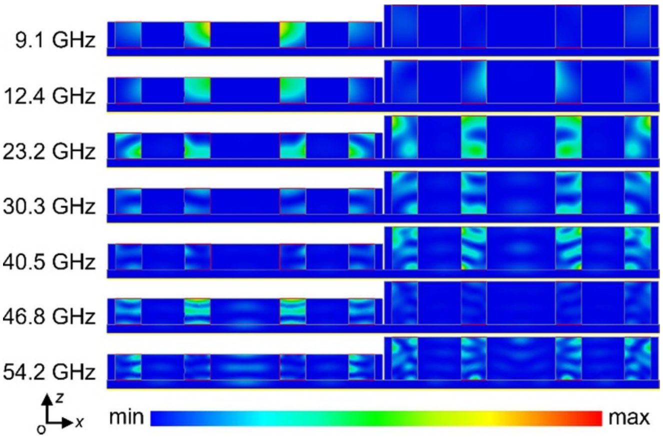

Figure 11. The energy loss density distribution of the C-A ILMMA at the peak frequency of 9.1 GHz, 12.4 GHz, 23.2 GHz, 30.3 GHz, 40.5 GHz, 46.8 GHz and 54.2 GHz respectively in *x–z* cutting planes along with the magnetic field orientation.

At lower frequency (9.1 GHz and 12.4 GHz), the low cylindrical groove predominantly contributes to the absorber's absorption, with the IL playing a pivotal role relative to the photosensitive resin. Loop-shaped magnetic field lines mainly manifest within the inner and outer IL rings of the low cylindrical groove. These configurations, acting as electric dipoles to introduce potent electric resonances, and the relevant energy loss distribution are depicted in figure 11.

As the frequency escalates (23.2 GHz, 30.3 GHz, 40.5 GHz, 46.8 GHz and 54.2 GHz), the central cylindrical photosensitive resin and the inner and outer photosensitive resin rings, akin to a 'visual bridge,' interconnect with the IL ring, forming additional loop-shaped magnetic field lines. Consequently, the losses from the photosensitive resin become increasingly

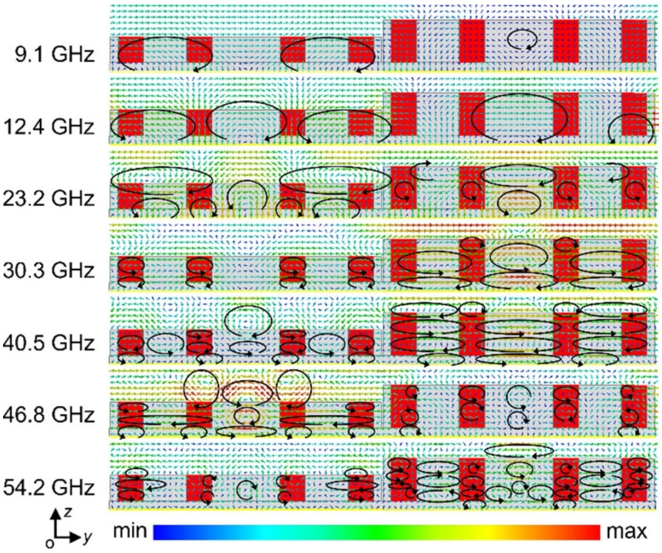

Figure 12. The electric field distribution of the C-A ILMMA at the peak frequency of 9.1 GHz, 12.4 GHz, 23.2 GHz, 30.3 GHz, 40.5 GHz, 46.8 GHz and 54.2 GHz respectively in *y–z* cutting planes along with the electric field orientation.

significant. Meanwhile, the high cylindrical groove also contributes to the absorber's absorption and the number of the loop-shaped magnetic field lines within the inner and outer IL rings of the high cylindrical groove increases as increasing frequency. In addition, the inner and outer IL rings of the low and high cylindrical groove, combined with the central and bottom cylindrical photosensitive resin, form closed magnetic field loops. This observation aligns with the energy loss density distribution depicted in figure 11.

Figure 12 delineates the electric field distribution of the C-A ILMMA. At the observed peaks, loop-shaped electric field lines emerge, functioning analogously to magnetic dipoles and inducing magnetic resonances.

At lower frequency (9.1 GHz and 12.4 GHz), similar to magnetic field distribution presented in figure 10, loop-shaped electric field lines appear within the inner and outer IL rings of the low cylindrical groove, inducing magnetic resonances, mainly contribute to the absorber's absorption. It is worth noting that a singular, albeit weak, loop-shaped electric field line manifests in the central cylindrical photosensitive resin of the high cylindrical groove, this is different from that in magnetic field distribution.

At higher frequency (23.2 GHz, 30.3 GHz, 40.5 GHz, 46.8 GHz and 54.2 GHz), the high cylindrical groove also contributes to the absorber's absorption and the number of the loop-shaped electric field lines within the inner and outer IL rings of both low and high cylindrical grooves increases as increasing frequency. At the same time, the role of photosensitive resins is no longer ignored. Clearly, some loop-shaped electric field lines are discerned in the central cylindrical photosensitive resin, and the bottom photosensitive resin in conjunction with the inner and outer IL rings also forms some closed electric field loops. These electric field configurations function as magnetic dipoles, inducing strong magnetic resonances, as corroborated by the energy loss density distribution presented in figure 13.

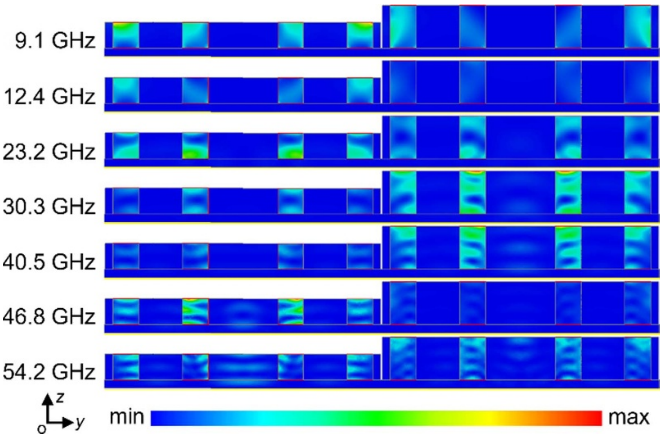

Figure 13. The energy loss density distribution of the C-A ILMMA at the peak frequency of 9.1 GHz, 12.4 GHz, 23.2 GHz, 30.3 GHz, 40.5 GHz, 46.8 GHz and 54.2 GHz respectively in *y–z* cutting planes along with the electric field orientation.

In the analysis of the C-A ILMMA's electric and magnetic field distributions, it is evident that the primary energy loss stems from two sources: ohmic loss due to electrical resonance and dielectric loss from magnetic resonance. These resonances, closely aligned in frequency, coalesce to produce a broadband absorption characteristic of the C-A ILMMA. Central to this absorption phenomenon is the role of the IL, which can be attributed to the intricate microscopic structure of [Emim][N(CN)$_2$]. The IL is a complex medium, comprising ion clusters, anion–cation pairs that form electric dipoles, and a significant presence of free ions, which contribute to the induced ionic current. Upon exposure to an external electromagnetic field, the IL's electric dipoles undergo polarization, oscillating in tandem with the electric field. Concurrently, the free ions' movement generates an induced ionic current. This behavior is corroborated by the magnetic and electric field distributions depicted in figures 10 and 12. Consequently, electromagnetic energy undergoes dissipation, primarily through dielectric and ohmic losses, which is then transformed into heat energy. It is imperative to note that, at higher frequencies, the influence of the photosensitive resin on the C-A ILMMA's absorption becomes increasingly significant. As illustrated in figures 10 and 12, the photosensitive resin acts as a cohesive 'bond', linking the foundational 'atom' (IL) to construct the holistic 'molecule' (C-A ILMMA), thereby facilitating robust absorption.

3.5. Experimental verification and comparative analysis

A 3D structural scaffold, measuring 256 × 256 mm^2 and depicted in figure 14(a), was fabricated in accordance with the optimized geometrical parameters of the C-A ILMMA. The IL [Emim][N(CN)$_2$] used in experiment were synthesized in our cooperative laboratory (Lanzhou Institute of Chemical

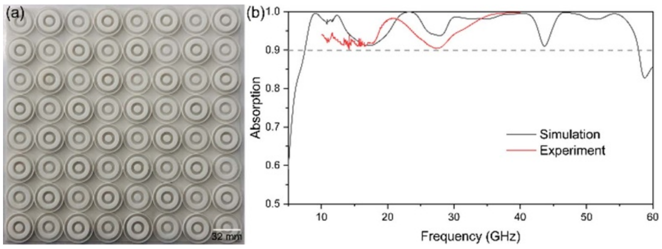

Figure 14. The top view of the C-A ILMMA in (a) and the comparison of absorption spectra between simulated and experimental results of the C-A ILMMA in (b).

Table 1. Comparison of absorption performance between the C-A ILMMA in this work and previous ILs-based ultra-broadband absorber.

Absorption bandwidth (GHz)	Relative bandwidth	References
20.6	110.2%	[28]
36.1	113.0%	[30]
39.7	136.2%	[31]
50.3	154.1%	This work

Physics, Chinese Academy of Sciences, China), and the purity is >99% and aqueous content <1000 ppm. The IL [Emim][N(CN)$_2$] was meticulously injected into the scaffold's single cylindrical groove, which features both an inner and an outer ring of vacant slots, until full saturation was achieved. The absorption performance of the C-A ILMMA was subsequently evaluated using an Agilent E8363B vector network analyzer, coupled with a pair of standard broadband linearly polarized horn antennas. All experimental measurements were conducted in a controlled microwave darkroom environment.

As depicted in figure 14(b), the C-A ILMMA exhibited an absorption efficiency exceeding 90% within the frequency range of 10–40 GHz, while the deviation between the simulated and experimental results could be caused by slight change of the IL volume at low frequency and increased susceptibility to mismachining tolerance at high frequencies. It is noteworthy that the experimental data could not be extended to the 40–60 GHz range due to the limitations inherent to the Agilent E8363B Vector Network Analyzer employed. However, based on the observed performance, it is reasonable to extrapolate that the C-A ILMMA would maintain optimal absorption characteristics across the entire frequency spectrum under investigation.

A comparative evaluation of the C-A ILMMA developed in this work and previously published IL-based ultra-broadband ILMMA designs was conducted, focusing on effective and relative absorption bandwidths calculated according to equations (6) and (9) respectively. As summarized in table 1, both the effective and relative absorption bandwidths of the C-A ILMMA surpass those of absorbers presented in prior work. The exceptional ultra-broadband performance of the C-A ILMMA can be attributed to the strategic injection of [Emim][N(CN)$_2$] into the C-A designed cylindrical groove. The C-A ILMMA not only demonstrates superior absorption capabilities but also sets a new benchmark in the realm of ultra-broadband metamaterial absorbers, thereby validating the efficacy of the C-A design and the choice of IL.

4. Conclusion

In this work, the IL [Emim][N(CN)$_2$], characterized by a high dielectric loss factor and superior conductivity, was identified as a promising absorbing material. This was subsequently utilized to construct an ILMMA, underpinned by the innovative concept of the C-A design. Numerical analyses reveal that the proposed C-A ILMMA achieves absorption rates exceeding 90% across a frequency spectrum of 7.5–57.0 GHz, culminating in a relative absorption bandwidth of 153%. Owing to its symmetrical structural design, the C-A ILMMA demonstrates polarization insensitivity, effectively operating across a broad range of polarization angles from 0° to 90°. Furthermore, even with an increased incident angle of 60°, the C-A ILMMA sustains absorption rates above 85% within the frequency bands of 9.0–13.3 GHz and 24.7–60.0 GHz, underscoring its wide-angle absorption capabilities.

A meticulous exploration into the temperature-dependent behavior of the C-A ILMMA's absorption revealed a nuanced trend. Specifically, as the temperature escalates from 20 °C to 100 °C, there is a discernible decline in the absorption rate between 9.1 GHz and 12.4 GHz. However, even under these conditions, the absorption rate remains commendably above 90%. Concurrently, a subtle augmentation in the absorption bandwidth is observed with rising temperatures. The underlying mechanism for the observed electromagnetic energy dissipation in the C-A ILMMA can be traced back to dielectric and ohmic losses, which are transmuted into thermal energy. This phenomenon is predominantly driven by the potent macroscopic magnetic and electric resonances, which, in turn, are attributed to the polarizable electric dipoles in the IL that oscillate in response to external electric fields and the induced ionic currents stemming from the mobility of free ions and charged ion clusters at the microscopic scale.

Corroborating the aforementioned findings, experimental evaluations further substantiate the efficacy of the C-A ILMMA. The absorber consistently exhibits an absorptivity rate surpassing 90% over an ultra-broadband frequency range spanning from 10 to 40 GHz. This observation harmoniously aligns with the preceding numerical predictions, reinforcing the robustness and potential applicability of the C-A ILMMA in relevant domains.

Data availability statement

All data that support the findings of this study are included within the article (and any supplementary files).

Acknowledgments

The authors acknowledge the financial support of this work from the Fund for Less Developed Regions of the National Natural Science Foundation of China (62061025), Natural Science Foundation of Gansu Province for Young Scientists

(23JRRA1112) and the Scientific Research Foundation of Lanzhou University for the Talented Young Scholars (561120207).

ORCID iDs

Yongji Guan https://orcid.org/0000-0001-9210-3530
Fulong Yang https://orcid.org/0000-0003-3307-1190
Xiaoping Zhang https://orcid.org/0000-0003-0046-211X

References

[1] Wen J, Zhao Q, Peng R, Yao H, Qing Y, Yin J and Ren Q 2022 Progress in water-based metamaterial absorbers: a review *Opt. Mater. Express* **12** 1461–79

[2] Andryieuski A, Kuznetsova S M, Zhukovsky S V, Kivshar Y S and Lavrinenko A V 2015 Water: promising opportunities for tunable all-dielectric electromagnetic metamaterials *Sci. Rep.* **5** 13535

[3] Zhou Q, Liu H, Gu Y, Duan W, Liu X, Ye F, Fan X and Du L 2024 3D printed PyC/Al_2O_3 ceramic metamaterials with different micro-channels for tunable microwave absorption *J. Eur. Ceram. Soc.* **44** 270–6

[4] Zhou Q, Shi T, Xue B, Gu S, Ren W, Ye F, Fan X and Du L 2023 Multi-scale integrated design and fabrication of ultra-broadband electromagnetic absorption utilizing multi-walled carbon nanotubes-based hierarchical metamaterial *Compos. Sci. Technol.* **232** 109877

[5] Zhou Q, Qi C, Shi T, Li Y, Ren W, Gu S, Xue B, Ye F, Fan X and Du L 2023 3D printed carbon based all-dielectric honeycomb metastructure for thin and broadband electromagnetic absorption *Composites* A **169** 107541

[6] Silalahi H M, Chiang W-F, Shih Y-H, Wei W-Y, Su J-Y and Huang C-Y 2022 Folding metamaterials with extremely strong electromagnetic resonance *Photon. Res.* **10** 2215–22

[7] Liu S, Xu F, Zhan J, Qiang J, Xie Q, Yang L, Deng S and Zhang Y 2022 Terahertz liquid crystal programmable metasurface based on resonance switching *Opt. Lett.* **47** 1891–4

[8] Li S J, Li Y B, Zhang L, Luo Z J, Han B W, Li R Q, Cao X Y, Cheng Q and Cui T J 2021 Programmable controls to scattering properties of a radiation array *Laser Photon. Rev.* **15** 2000449

[9] Chai M, Wang Y, Chen C, Zhao Z, Jin M and He T 2022 Metamaterials-based photoelectric conversion: from microwave to optical range *Laser Photon. Rev.* **16** 2100458

[10] Luque-González J M, Ortega-Moñux A, Halir R, Schmid J H, Cheben P, Molina-Fernández Í and Wangüemert-Pérez J G 2021 Bricked subwavelength gratings: a tailorable on-chip metamaterial topology *Laser Photon. Rev.* **15** 2000478

[11] Ahmadivand A and Gerislioglu B 2022 Photonic and plasmonic metasensors *Laser Photon. Rev.* **16** 2100328

[12] Kwon H, D'Aguanno G and Alú A 2021 Optically transparent microwave absorber based on water-based moth-eye structures *Opt. Express* **29** 9190–8

[13] Zhang Y, Dong H, Mou N, Li H, Yao X and Zhang L 2021 Tunable and transparent broadband metamaterial absorber with water-based substrate for optical window applications *Nanoscale* **13** 7831–7

[14] Shen Y, Zhang J, Pang Y, Wang J, Ma H and Qu S 2018 Transparent broadband metamaterial absorber enhanced by water-substrate incorporation *Opt. Express* **26** 15665–74

[15] Yoo Y J, Ju S, Park S Y, Kim Y J, Bong J, Lim T, Kim K W, Rhee J Y and Lee Y 2015 Metamaterial absorber for electromagnetic waves in periodic water droplets *Sci. Rep.* **5** 14018

[16] Pang Y, Shen Y, Li Y, Wang J, Xu Z and Qu S 2018 Water-based metamaterial absorbers for optical transparency and broadband microwave absorption *J. Appl. Phys.* **123** 155106

[17] Wang Q, Bi K and Lim S 2020 All-dielectric transparent metamaterial absorber with encapsulated water *IEEE Access* **8** 175998–6004

[18] Song Q *et al* 2017 Water-resonator-based metasurface: an ultrabroadband and near-unity absorption *Adv. Opt. Mater.* **5** 1601103

[19] Wu Z, Chen X, Zhang Z, Heng L, Wang S and Zou Y 2019 Design and optimization of a flexible water-based microwave absorbing metamaterial *Appl. Phys. Express* **12** 057003

[20] Zhang X, Yan F, Du X, Wang W and Zhang M 2020 Broadband water-based metamaterial absorber with wide angle and thermal stability *AIP Adv.* **10** 055211

[21] Shen Y, Zhang J, Pang Y, Zheng L, Wang J, Ma H and Qu S 2018 Thermally tunable ultra-wideband metamaterial absorbers based on three-dimensional water-substrate construction *Sci. Rep.* **8** 4423

[22] Pang Y, Wang J, Cheng Q, Xia S, Zhou X Y, Xu Z, Cui T J and Qu S 2017 Thermally tunable water-substrate broadband metamaterial absorbers *Appl. Phys. Lett.* **110** 104103

[23] Xie J, Quader S, Xiao F, He C, Liang X, Geng J, Jin R, Zhu W and Rukhlenko I D 2019 Truly all-dielectric ultrabroadband metamaterial absorber: water-based and ground-free *IEEE Antennas Wirel. Propag. Lett.* **18** 536–40

[24] Ren J and Yin J Y 2018 Cylindrical-water-resonator-based ultra-broadband microwave absorber *Opt. Mater. Express* **8** 2060–71

[25] Xiong H and Yang F 2020 Ultra-broadband and tunable saline water-based absorber in microwave regime *Opt. Express* **28** 5306–16

[26] Li S, Shen Z, Yang H, Liu Y, Yang Y and Hua L 2021 Ultra-wideband transmissive water-based metamaterial absorber with wide angle incidence and polarization insensitivity *Plasmonics* **16** 1269–75

[27] Shen Z, Huang X, Yang H, Xiang T, Wang C, Yu Z and Wu J 2018 An ultra-wideband, polarization insensitive, and wide incident angle absorber based on an irregular metamaterial structure with layers of water *J. Appl. Phys.* **123** 225106

[28] Zhou Y, Shen Z, Huang X, Wu J, Li Y, Huang S and Yang H 2019 Ultra-wideband water-based metamaterial absorber with temperature insensitivity *Phys. Lett.* A **383** 2739–43

[29] Chen Y, Chen K, Zhang D, Li S, Xu Y, Wang X and Zhuang S 2021 Ultrabroadband microwave absorber based on 3D water microchannels *Photon. Res.* **9** 1391–6

[30] Zhou Y, Shen Z, Wu J, Zhang Y, Huang S and Yang H 2020 Design of ultra-wideband and near-unity absorption water-based metamaterial absorber *Appl. Phys.* B **126** 1–5

[31] Zhang X, Zhang D, Fu Y, Li S, Wei Y, Chen K, Wang X and Zhuang S 2020 3D printed swastika-shaped ultrabroadband water-based microwave absorber *IEEE Antennas Wirel. Propag. Lett.* **19** 821–5

[32] Xie J, Zhu W, Rukhlenko I D, Xiao F, He C, Geng J, Liang X, Jin R and Premaratne M 2018 Water metamaterial for ultra-broadband and wide-angle absorption *Opt. Express* **26** 5052–9

[33] Welton T 2018 Ionic liquids: a brief history *Biophys. Rev.* **10** 691–706

[34] Plechkova N V and Seddon K R 2008 Applications of ionic liquids in the chemical industry *Chem. Soc. Rev.* **37** 123–50

[35] Armand M, Endres F, MacFarlane D R, Ohno H and Scrosati B 2010 Ionic-liquid materials for the electrochemical challenges of the future *Materials for Sustainable Energy* (Macmillan Publishers Ltd) pp 129–37

[36] Earle M J, Esperança J M S S, Gilea M A, Canongia Lopes J N, Rebelo L P N, Magee J W, Seddon K R and Widegren J A 2006 The distillation and volatility of ionic liquids *Nature* **439** 831–4

[37] Gong J, Yang F, Shao Q, He X, Zhang X, Liu S, Tang L and Deng Y 2017 Microwave absorption performance of methylimidazolium ionic liquids: towards novel ultra-wideband metamaterial absorbers *RSC Adv.* **7** 41980–8

[38] Yang F, Gong J, Yang E, Guan Y, He X, Liu S, Zhang X and Deng Y 2019 Microwave-absorbing properties of room-temperature ionic liquids *J. Phys. D: Appl. Phys.* **52** 155302

[39] Yang F, Gong J, Yang E, Guan Y, He X, Liu S, Zhang X and Deng Y 2019 Ultrabroadband metamaterial absorbers based on ionic liquids *Appl. Phys.* A **125** 149

[40] Yang E, Yang F, Pei J, Zhang X, Liu S and Deng Y 2019 All-dielectric ultra-broadband metamaterial absorber based on imidazole ionic liquids *J. Phys. D: Appl. Phys.* **52** 395501

[41] Yang F, Zhang C, Zhang A, Zhu X, Xu H and Wang D 2022 Thermally tunable broadband metamaterial absorbers based on ionic liquids *Opt. Express* **30** 45883–94

[42] Zhang C, Yang F, Zhang A, Zhu X, Xu H and Wang D 2023 An ionic liquid-based ultra-broadband absorber with temperature stability, polarization insensitivity, and wide incident angle *J. Phys. D: Appl. Phys.* **56** 085501